Journal of Nuclear Science and Technology

ISSN: 0022-3131 (Print) 1881-1248 (Online) Journal homepage: https://www.tandfonline.com/loi/tnst20

Nondestructive Determination of Fresh and Spent Nuclear Fuel Rod Density Distributions through Computerised Gamma-Ray Transmission Tomography

Stefano CARUSO , Michael F. MURPHY , Fabian JATUFF & Rakesh CHAWLA

To cite this article: Stefano CARUSO , Michael F. MURPHY , Fabian JATUFF & Rakesh CHAWLA (2008) Nondestructive Determination of Fresh and Spent Nuclear Fuel Rod Density Distributions through Computerised Gamma-Ray Transmission Tomography, Journal of Nuclear Science and Technology, 45:8, 828-835, DOI: 10.1080/18811248.2008.9711484

To link to this article: https://doi.org/10.1080/18811248.2008.9711484

Journal of NUCLEAR SCIENCE and TECHNOLOGY, Vol. 45, No. 8, p. 828–835 (2008)

ARTICLE

Nondestructive Determination of Fresh and Spent Nuclear Fuel Rod Density Distributions through Computerised Gamma-Ray Transmission Tomography

Stefano CARUSO[1,2,*,†], Michael F. MURPHY[1], Fabian JATUFF[1] and Rakesh CHAWLA[1,2]

[1]*Laboratory for Reactor Physics and Systems Behaviour, Paul Scherrer Institute, CH-5232 Villigen PSI, Switzerland*
[2]*Ecole Polytechnique Fédérale de Lausanne (EPFL), CH-1015 Lausanne, Switzerland*

(Received January 24, 2008 and accepted in revised form April 25, 2008)

The morphology of single PWR UO_2 fuel rods has been investigated by employing computerised gamma-ray transmission tomography. Four highly burnt fuel rods of different burnups (from 52 GWd/t to 126 GWd/t) and a fresh rod have been investigated. This paper describes the tomographic station built to acquire the projections together with the related experimental procedure, followed by the description of the image reconstruction techniques implemented. The principal results obtained are presented and analysed at three levels. First, the derived linear attenuation coefficient matrix, which is very useful for the implementation of emission tomography, is discussed. Second, the variation of density as a function of rod radius is presented, showing an interesting morphological change of the fuel with burnup. Particularly for the highest burnup sample, the periphery is characterised by a lower density (a steep decrease of almost 10% from the adjacent region) characteristic of an ultrahigh-burnup high-porosity structure. Finally, the nondestructive derivation of the volume-averaged fuel density was performed, compared with other experimental data, and plotted as a function of burnup, so that an interesting linear relationship between density and burnup was established, providing a potential indicator for the noninvasive determination of nuclear fuel rod burnup.

KEYWORDS: transmission tomography, nondestructive techniques, fuel density, high burnup, spent fuel, light water reactors

I. Introduction

In the process of evaluating nuclear fuel performance, different types of nondestructive methods have been characterised and applied, *e.g.*, gamma-ray spectrometry,[1)] neutron measurements,[2)] and reactivity and calorimetric measurements.[3)] Thus, the development, application, and validation of suitable experimental techniques of investigation play a very important role. For example, the implementation of computer tomography, widely used in medical applications, is a noninvasive technique that can be employed successfully in the investigation of single fuel rods as well as entire fuel assemblies. This technique, although not new in nuclear fuel characterisation,[4–9)] is a growing area due to the continued progress of computer science that makes possible the implementation of more sophisticated and better performing algorithms for the reconstruction of images.

Computerised tomography, in essence, is the reconstruction of an internal image of an object from external observations. In particular, the aim of transmission tomography is to obtain information regarding the nature and position of materials inside a body, using the absorption of a physical entity (gamma ray, X-ray, light, ultrasound) crossing the body itself. In contrast, emission tomography uses the observation of events that originate from inside the body.

In the case of transmission tomography applied to nuclear fuels, this technique can be considered both as a nondestructive analysis method for fuel rod density investigations and as a way to determine within-rod spatial distribution matrices of the linear attenuation coefficient. This technique was applied previously to radioactive waste packages,[6,7)] but not to irradiated fuel rods as investigated here.

In this work, the applied procedures and results obtained for the gamma-transmission tomography conducted on burnt and fresh fuel samples, previously deployed in the LWR-PROTEUS Phase II experiments,[10)] are presented. A fresh, 400-mm-long UO_2 segment containing 3.5% by weight ^{235}U and four burnt PWR UO_2 fuel rod segments also of 400 mm length, two with very high (52 GWd/t and 71 GWd/t) and two with ultrahigh (91 GWd/t and 126 GWd/t) pellet-averaged burnup values, have been investigated. The burnt samples have about 10 years of cooling

*Corresponding author, E-mail: stefano.caruso@nok.ch
†Present address: *Nordostschweizerische Kraftwerke AG, Kernkraftwerk Beznau, CH-5312 Döttingen, Switzerland. Tel. +41 56 266 6408.*

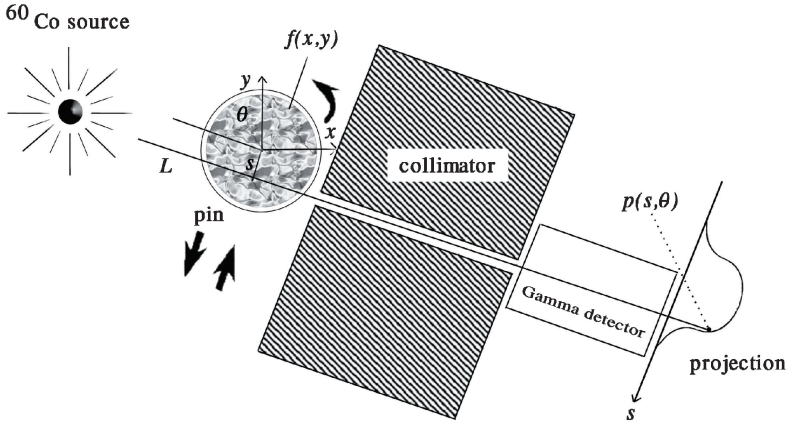

Fig. 1 Schematic illustration of the basic principles of the tomographic station. The fuel rods under investigation have a central UO_2 region of 9.14 mm diameter (before fuel swelling), the original cladding with external diameter of 10.76 mm, and a Zircaloy overcladding with internal and external diameters of 11.2 and 11.8 mm, respectively, the internal void being filled with helium.

time in the first three cases and 4 years in the last case. All the rod segments were encapsulated in Zircaloy overcladding (300–400 μm in thickness) to prevent their being damaged and to guard against contamination, the gap between the cladding and overcladding being filled with helium at 200 kPa. A new tomographic cell station was designed, built, and used for these investigations.

Section II gives a brief description of the experimental procedure, with the tomographic cell station and the currently applied procedures for transmission tomography reconstruction. The principal results obtained in terms of reconstructed 2D images of linear attenuation coefficient matrices are presented in Sec. III-1, whilst within-rod fuel material density distributions and volume-averaged densities are reported in Secs. III-2 and III-3, respectively. Final conclusions are given in Sec. IV.

II. Experimental Procedure

1. Tomography Working Principles

The basic requirement for a tomographic station is the ability to generate cross-sectional images of an object—a fuel rod in this case—on the basis of measurements of γ-rays emitted by, or transmitted through, separate "slices" of this object. For this reason, it is necessary to traverse the fuel rod laterally with respect to the collimator slit, making many steps across the whole width of the fuel rod and measuring the intensity of the γ-rays at each step. The set of intensity data collected for all the steps of a particular traverse is called a projection (see **Fig. 1**). In order to reconstruct the "image" of the object, a number of projections need to be recorded. This is done by rotating the object around its central axis and collecting the projections at different angular positions.

As indicated in Fig. 1, the tomographic station can operate in two different ways: using an external γ-source, such that the projections coming from the source can give information about the internal morphology of the object (transmission), or without the external source, such that the projections collected belong only to the internal source distribution (emission), giving information about the within-rod activity distribution $f(x, y)$. Here, only the procedures relevant to transmission tomography are detailed; the description of the emission tomography will be published separately.

2. Tomographic Cell Station

The measurement station, built at the zero-power research reactor PROTEUS of the Paul Scherrer Institute, is an installation specifically designed for the nondestructive investigation of highly active spent fuel rod segments of 400 mm length, primarily for high-resolution and single-emission transmission tomography. The station is a structure consisting of a lead shielding enclosure, a tungsten collimator, a remote handling system with the associated control system, a high-purity germanium (HPGe) detector with a support for the cryostat, a system for the injection of an external gamma source, and a set of neutron detectors. It is operated in combination with the PROTEUS transport flask/sample changer,[10] which loads an individual fuel segment into the station from the top, after which a remotely controlled clamping system ensures that the sample is secured in an accurately known position by means of a 'V' channel (see **Fig. 2**).

The collimator is a block of tungsten of 150 mm length with an internal slit of 0.2×20 mm, with a capability to modify the slit width if required. The lead shielding enclosure, 200 mm thick, was designed to host the remote clamping system. The latter is mounted on a base plate, which can be moved by a system of gears and stepping motors to traverse the sample past the collimator and to rotate it to different angular positions.

The gamma measurement equipment consists of an EG&G ORTEC HPGe coaxial detector, which has an 18% relative efficiency and a 1.67 keV resolution for the 1332 keV ^{60}Co photopeak. The HPGe is shielded with a cadmium and copper casing to stop the X-ray fluorescence produced in the lead. The detector is connected to an EG&G ORTEC DSPec Plus digital gamma-ray spectrometer,[11] a comprehensive unit containing an analogue-to-digital con-

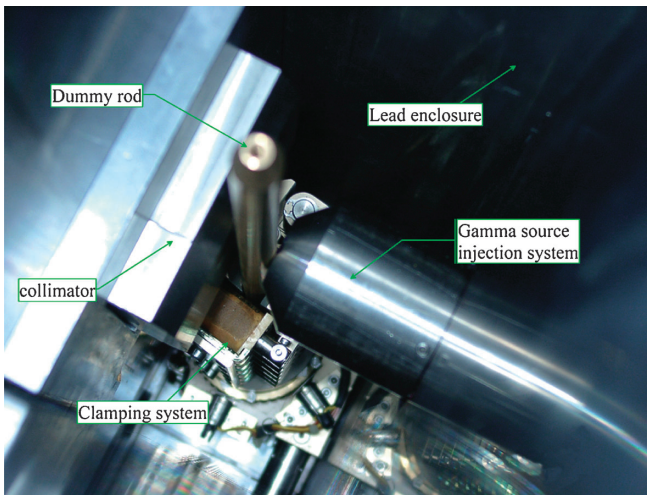

Fig. 2 View from the top of the internal part of the shielding. The gamma projector device terminal, the dummy rod gripped into the clamping system, and the tungsten collimator are shown.

verter, a digital shaping amplifier, and high-voltage power supply. The spectra acquisition and analysis software is the Gamma-Vision multichannel analyser program from EG&G ORTEC.[12] A lead filter of 30 mm thickness was placed in front of the detector, to attenuate effectively the low-energy scattered gammas and consequently to reduce the detector dead time.

As a fundamental requirement for transmission tomography measurements, a γ-source must be driven into the internal cavity of the station. For this purpose, a commercial gamma projector was rented and used for the measurements. Model Delta 880 of CONTROLTECH[13] is a compact exposure device normally used for industrial gamma radiography. It is designed to host different source types and projects the source through a guide tube of 2 m length. The gamma-ray projector body is made of depleted uranium and weighs 22 kg.

The γ-source used was ^{60}Co with a total activity of 2412 MBq (65.2 mCi) and dimensions of 1 mm diameter by 2 mm length. In order to use the cobalt source with the gamma projector in the tomography station, a special device was built. This device allows the penetration of the source guide tube into the enclosure shielding and ensures that the location of the source in the final position is as close as possible to the sample and in line with the collimator slit opening. Figure 2 shows the view from the top of the internal part of the shielding enclosure during a cold test campaign, with the gamma projector device terminal, the dummy rod gripped in the clamping system, and the tungsten collimator.

3. Projections Acquisition and Sinograms

High-resolution γ-spectrometry is the basis of the tomographic investigations illustrated here. The methodology used for the photopeak treatment, particularly for the need to derive the non-Gaussian gamma-peak areas properly, has been fully described in available reports[14,15] and is thus not repeated here.

Transmission tomography was employed in each case by measuring the relative intensities of the 1.173 and 1.332 MeV gamma rays produced by the external ^{60}Co source. Thus, photons emitted by the ^{60}Co, together with photons from long-lived gamma-emitting fission products present in the burnt samples, were recorded using an HPGe detector, for different lateral positions s and angular positions θ of the sample (see Fig. 1). Each recorded spectrum was analysed in order to derive, for each measurement step, the count rate corresponding to the different γ-lines of interest.

Each session of tomographic investigations comprised a total number of measurements $[k \times m]$, where k is the number of lateral displacements of the rod with respect to the collimator slit and m the number of rotations of the rod. In each case, the lateral step size used was 0.2 mm and the angular interval was 45°. The acquisition time of each single measurement $p(s, \theta)$ was between 10–20 min, with $m = 8$ and k typically ~60.

Once the projections had been acquired and corrected for count time and for slight mechanical deviations of the clamping system, the final sinograms were obtained. A sinogram is a suitable way to store the projections for image reconstruction. A single projection view $p(s, \theta)$, corresponding to parallel lines relative to a specific angle, is stored in the sinogram as a single column for all s measured. Each column in the sinogram consists of the projection views at a given angle. In practice, this means a change in domain from a Cartesian $\langle xy \rangle$ system to a polar $\langle s\theta \rangle$ system.

4. Image Reconstruction Procedure

As already mentioned, in transmission tomography, beams of radiation are passed through the body being investigated, from various positions and at various angles. Each beam is detected on the side of the body opposite from the beam source, and its detected intensity is compared with its unattenuated intensity. These data are collected at various angles, from 0 to 360 degrees. The property that is computed in transmission tomography is the linear attenuation coefficient, at various points in the object's cross section.

The body, *viz.*, the fuel rod, can be assumed to be a regular cylinder. Considering the intensity of the emitted beam I_0, the intensity I of the detected beam is $I_0 \cdot e^{-T}$, where the function T, the transmittance of the object, is given as

$$\ln(I_0/I) = T(s, \vartheta) = \int_L \mu_l(x, y) dl, \tag{1}$$

where $\mu_l(x, y)$ is the linear attenuation coefficient of the object at the point (x, y) and L is the line along which the beam travels.

Theoretically, any problem concerning reconstruction from projections is an ill-posed problem, because the analytical approach needs an infinite number of measured projections as input, which is unreasonable in practice. Nevertheless, this problem has been studied over many years in a large number of scientific, medical and technical fields, so that many different techniques have been developed. The

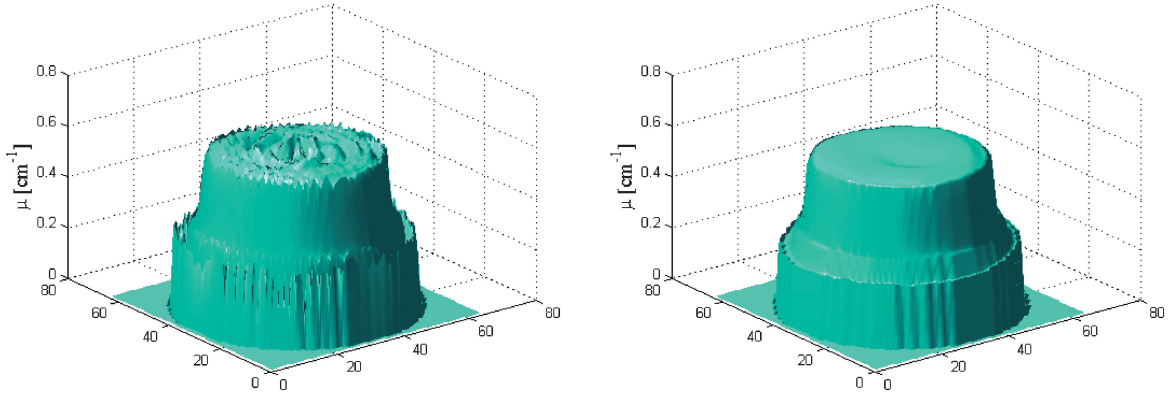

Fig. 3 Within-rod linear attenuation coefficient distribution (64 × 64 pixels) $\mu_l(x, y)$ [cm^{-1}] for the 52 GWd/t sample. Filtered-Back-Projection image (left) and Paraboloidal-Surrogates Coordinate Ascent Penalised Maximum Likelihood image (right).

approach followed in this work is based on several of these methods, and may be summarised in two main steps: first, an analytical method, filtered back-projection (FBP),[16] was used to generate a first-guess image. Then, an iterative statistical method, penalised maximum-likelihood expectation maximisation (PML) for transmission tomography,[17] was used to iterate on the first-guess noisy image and to generate the final linear attenuation coefficient matrix. In particular, this technique was integrated with a paraboloidal-surrogates coordinate ascent (PSCA) algorithm,[18] to accelerate the iterative convergence process. This approach was found to perform very well for the present work.

In brief, the filtered back-projection method consists of taking the inverse of the Radon transform of the function $T(x, y)$, which represents the unknown linear attenuation function. Because the Radon transform is given by the collection of the line integrals of the function T, which are indeed our measured projections, it is possible to calculate its inverse.[19] Effectively, the image is first back-projected and then filtered with a two-dimensional ramp filter.

The iterative method used, *i.e.*, the penalised maximum-likelihood expectation maximisation, is based on maximum-likelihood expectation-maximisation (ML-EM) techniques,[20,21] where a penalty term is included in the optimisation process. This penalty, or regularisation, term (accounting for a priori information such as smoothness) is added to the function to be maximised (objective function), and this is the specificity of the penalised ML-EM techniques,[17] as well as of all the so-called "penalised" methods. The objective function to be maximised is the difference in the log-likelihood ($L(\vec{f})$) and the penalty function ($R(\vec{f})$), the trade-off between the two being controlled by a parameter β:

$$\Phi(f) = \ln L(\vec{f}) - \beta R(\vec{f}). \tag{2}$$

β is a regularisation parameter that controls the trade-off between resolution and noise. It must be either estimated subjectively beforehand or calculated via an additional iterative process to be developed. Because the image noise increases with further iterations, the regularisation process becomes necessary to maintain this noise at a reasonably low level. A very interesting improvement of the penalised-likelihood image reconstruction technique, employed in this work, is the paraboloidal-surrogates coordinate ascent (PSCA) method.[18] In brief, it uses a global surrogate function for the original objective function, which is not separable but has a simple quadratic form, to accelerate the convergence, thus reducing the noise propagation. It has several variations, depending on how one chooses the parabola curvatures. For its application to nuclear fuel rods, a "fast pre-computed" curvature,[18] usually monotonic, is recommended.

The practical implementation of the computerised tomography was made with the Aspire 3.0 code, developed by J. Fessler at the University of Michigan.[22] This is a sparse iterative reconstruction library, for image reconstruction, which implements several reconstruction techniques, analytical and iterative, and allows the use of different penalties and resolution properties. Details about the current procedure are available elsewhere.[14]

III. Results and Discussion

The resolution of the images is 64 × 64, where each pixel width is 0.2 mm. The slit width of the collimator was fixed (uniform sampling) to be equal to the pixel width for all measurements (0.2 mm). All the images generated here are produced with the 1.332 MeV photopeak.

1. Attenuation Coefficient Matrices

Figure 3 shows the within-rod distribution of the linear attenuation coefficient $\mu_l(x, y)$ [in cm^{-1}] evaluated at the individual pixels, as derived for the 52 GWd/t sample. On the left is the FBP image, and on the right the PSCA-PML image. The FBP image is a noisy but realistic image. The noise was not immediately suppressed, to avoid alteration of the physical properties of the object (especially at the edge of the rod). The noise treatment is carried out using statistical methods. By using the PSCA algorithm, the noise is suppressed during the iterative process without compromising the validity of the reconstruction. By observing the PSCA-PML image, the difference in the attenuation

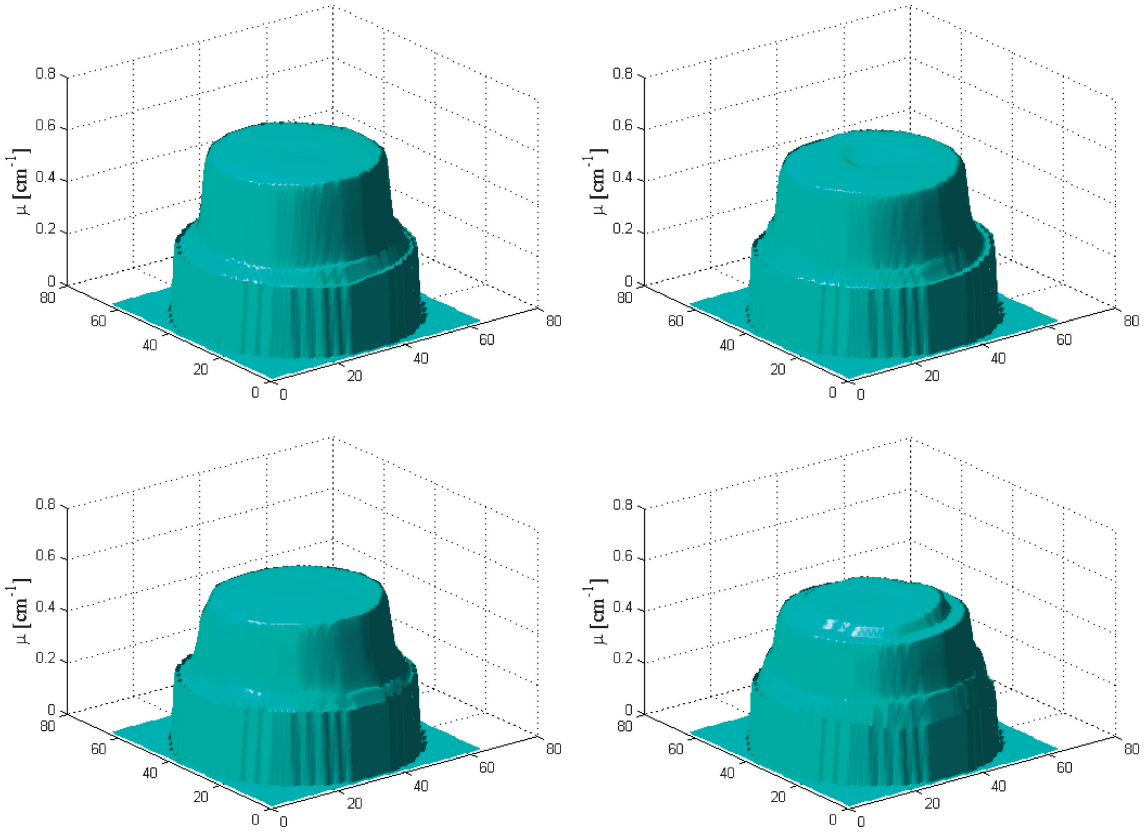

Fig. 4 Within-rod linear attenuation coefficient $\mu_l(x, y)$ [cm^{-1}] distribution for (a) fresh fuel, (b) 71 GWd/t, (c) 91 GWd/t, and (d) 126 GWd/t spent fuel segments, derived using the Paraboloidal-Surrogates Coordinate Ascent Penalised Maximum Likelihood algorithm.

values between the Zircaloy cladding material and the UO_2 fuel matrix becomes evident. From this image, it is not possible to distinguish very well the gap between the cladding and the overcladding. This is more visible after applying a higher resolution, which was introduced when the $\mu(l)$ image was converted to a density image, as shown in the next section.

The most important goal of the attenuation map is the investigation of inhomogeneities in the physical structure of the fuel matrix, in order to use these maps to apply appropriate attenuation corrections for further nondestructive studies such as emission tomography. In **Fig. 4**, the PSCA-PML images illustrate the linear attenuation reconstructions for (a) the fresh sample, and (b) to (d) for the spent fuel samples with burnups of 71, 91 and 126 GWd/t, respectively. These reconstructions have been obtained using an edge-preserving Huber penalty function with a "2^{nd}-order neighbourhood," and the trade-off parameter $\beta = 9$, performing a total of 30 iterations.

2. Density Distribution

The reconstruction was based on the same techniques and routine as those described in Sec. III-1, with the same penalty parameters, but changing the regularisation parameter β ($\beta = 7$) such that the noise is slightly increased in the final image as the resolution at the edge of the rod is improved. In this way, it was possible to better differentiate the overcladding from the cladding region. Because the collimator slit width is only 200 μm, it is not easy to distinguish regions of 125 μm (the gap between cladding and overcladding) or 300 μm (the thickness of the overcladding for the 126 GWd/t sample). The final density distribution $\rho(I, j)$ was derived from the reconstructed linear attenuation matrix $\mu_l(I, j)$ using the following formula:

$$\rho(i, j) = \frac{\mu_l(i, j)}{\mu_m} \tag{3}$$

where μ_m is the tabulated mass attenuation for the given material, and i, j the pixel indices.

In order to increase the displayed resolution, the image was converted from 64×64 to 128×128 pixels (pixel width of 100 μm) by simply splitting the original pixel into four pixels.

In **Fig. 5**, a vertical cut view of density distributions for all the samples, derived using azimuthally averaged sinograms, is shown. Here, the decrease in fuel density with burnup can be easily observed. The density of the cladding, which should be identical for all the cases, shows discrepancies between the samples. This is because the slit of 200 μm width cannot properly resolve the void zone between the cladding and the overcladding and, as a consequence, this region is seen as a mixture of Zircaloy and helium, producing, as a result, a lower density in the image. It is, however, possible from this plot to distinguish the overcladding and

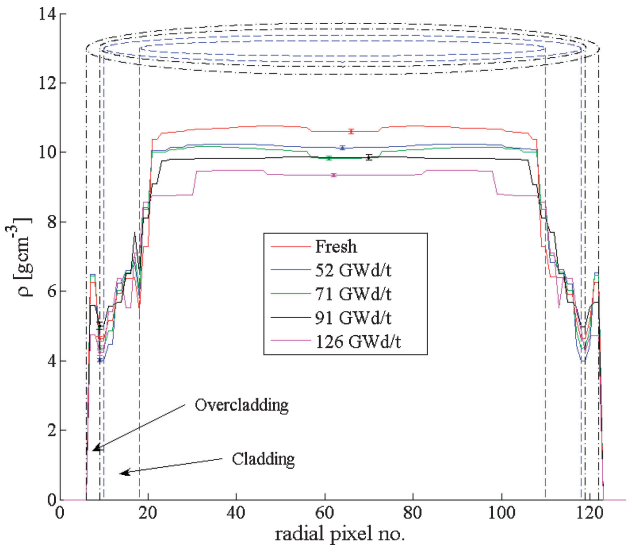

Fig. 5 Density [gcm^{-3}] distribution profiles for the various fuel rod samples. Each plot is a vertical cut view of density distribution derived with azimuthally averaged images. The original image has 128 × 128 pixels. Uncertainty bars are present for the central zone, and for the periphery (on the left side, between the cladding and overcladding). The actual dimensions of the cladding and overcladding are graphically shown (730 and 300 µm thick, respectively).

the cladding of the rod. The actual dimensions of the cladding and the overcladding are graphically illustrated in the same picture, to help in the comprehension of the results. It is worth noting that the gap between the pellet and cladding is expected to be completely closed for the samples investigated here, due to clad creep-down and the swelling of the pellets.

Special attention to the 126 GWd/t sample needs to be given here, which shows a very singular density profile. We can observe a lower density zone at the periphery of the fuel pellet, then a step with a higher density region (a factor of ~1.1 between the two), followed by a decrease in density going towards the centre of the rod. The radial extent of the lower density peripheral region (~1 mm) appears to correspond to a high-burnup-structure region with a much higher level of porosity such that it yields a lower overall density.[23)]

The uncertainty (1σ) in the central region is <0.7%, whilst the periphery is characterised by higher values (1.2%–2.5%, depending on the sample). These uncertainties, for the two distinct regions, central and peripheral, were derived from the results of a sensitivity study carried out as follows: First, noise was introduced into the input sinograms, so as to derive new sinograms using the relation

$$S_{noisy} = S_{clear}(1 + n\sigma P) \tag{4}$$

where S_{clear} is the sinogram without perturbation, σ is the statistical uncertainty of the measurements, n is the order of σ to be tested, and P is a Gaussian probability function, all in matrix form. The artificially noisy sinograms (S_{noisy}) were then processed, and the images so obtained compared with the image reconstructed without added noise.

3. Average Density vs. Burnup

The fuel rod average density was derived by directly using the data from the measured projections, without tomographic treatment. The density is derived from the calculation of the attenuation in the fuel, as well as in the cladding and overcladding:

$$I = I_0 \cdot \exp^{-\mu_{UO_2} x_{UO_2}} \cdot \exp^{-\mu_{zry} x_{zry}} \tag{5}$$

where I_0 is the intensity of the emitted beam, I is the intensity of the detected beam, μ is the linear attenuation coefficient in the fuel pellet (UO_2), and in the cladding and overcladding material (zry), x_{UO_2} and x_{zry} are the path lengths in UO_2 and Zircaloy, respectively.

The final density ρ is given as

$$\rho = -\ln\left(\frac{I}{I_0}\right) \cdot \frac{1}{x_{UO_2}\mu_{UO_2}(m)} \cdot \frac{1}{\exp^{-\mu_{zry} x_{zry}}}, \tag{6}$$

where $\mu(m)$ is the mass attenuation coefficient in the fuel pellet (UO_2).

The density derivation was made with the central 36 measurements, uniformly sampled by 0.2 mm steps, of each projection data set. The final value has been obtained as a weighted mean of all the projections. The uncertainty is an average sigma (σ) derived using the net measured counts, given as

$$\sigma_k = \sqrt{\left(\frac{1}{\sqrt{I_k}}\right)^2 + \left(\frac{1}{\sqrt{I_0}}\right)^2}, \tag{7}$$

where I_k is the net area measured at position k and I_0 is the net area measured directly with the beam (*i.e.*, without a sample in between). These two errors are added in quadrature, as the quotient of I_k/I_0 is the major term responsible for the total error. The currently assessed uncertainties are ≤0.6% for all the samples.

The average fuel density is plotted as a function of the burnup in **Fig. 6**. A clear decrease in density with burnup is observed. These results are compared with fuel density measurements for the two extreme cases, *viz.*, the manufacturer's data for the fresh sample and a PSI-Hotlab Archimedes measurement for the 126 GWd/t sample.[24)]

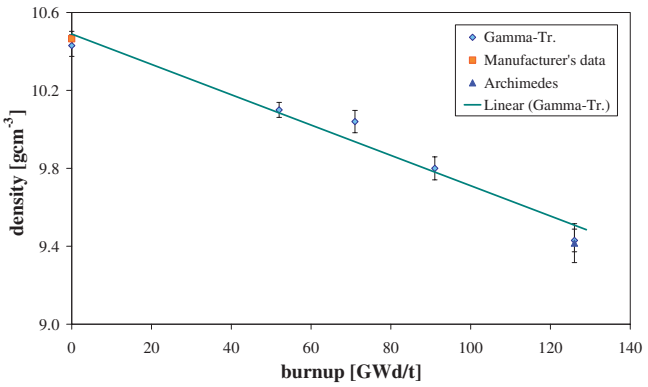

Fig. 6 Average fuel pellet density values from the current gamma transmission investigations (Gamma-Tr.), together with the results from a PSI-Hotlab Archimedes measurement for the 126 GWd/t sample (Archimedes) and from the manufacturer's data for the fresh sample (Manufacturer's data).

The agreement is seen to be excellent. Furthermore, the assumption of a linear relationship between the density and the burnup is seen to be reasonable, even after accounting for the known slight increase in density from re-sintering in fresh fuel at the beginning of irradiation.

IV. Conclusions

A gamma tomographic cell station has been designed, built, and used for gamma-transmission tomographic investigations performed on burnt and fresh PWR UO_2 fuel rod segments.

The application of transmission tomography to single fuel rods has been shown to be a feasible and interesting option to achieve the nondestructive determination of fuel density distributions. Interesting results have been produced, particularly for the 126 GWd/t sample, which shows a very singular density profile. A lower density zone at the periphery of the rod was observed, then a step with a higher density region (a factor of $\sim$10% between the two), followed by a decrease in density going towards the centre of the rod. The radial extent of this lower density peripheral region ($\sim$1 mm) seems to correspond to the high-burnup-structure region, with high porosity, as reported elsewhere.[23)]

Furthermore, because transmission tomography can be used in combination with emission tomography, a linear attenuation coefficient matrix was derived, to be employed in the emission reconstruction process, so as to increase the final image accuracy. This work has been already carried out[14)] and will be presented separately.

The currently acquired projections have also been used to determine the average densities of the fuel segments. The deduced values were compared with other experimental data and showed a high degree of consistency. Furthermore, a linear relationship between fuel density and burnup has been indicated, even after considering the slight pellet densification that occurs in fresh fuel at the beginning of irradiation in the core. It is relevant to note that, once the linear relationship between fuel density and burnup has been validated, one may eventually be able to evaluate the burnup directly from the current type of density assessment using gamma transmission.

Future developments that might further improve the experimental procedure described here would include a strategy focused on privileging the acquisition of projections at the periphery of the rod. For instance, reducing the slit width and the step size, and increasing the acquisition time of the spectra when measuring the rod periphery, may improve the resolution of the reconstructed image at the rod edge.

Furthermore, the tomographic measurements applied currently to UO_2 fuels may be extended to MOX fuels. The possibility of providing a noninvasive assessment of MOX fuel density variation with burnup would be of particular interest.

Acknowledgments

The LWR-PROTEUS programme is being conducted jointly by PSI and the Swiss Nuclear Power Plants. We are particularly grateful to H.-D. Berger (Framatome-ANP), J. Krouthén (NOK), G. Meier and P. Hirt (KKG), D. Furtado and U. Georg (BKW), and R. Brogli (PSI) for their strong support of the experiments. The authors would also like to express their gratitude to R. Seiler, M. Fassbind and M. W. Zimmermann of the PROTEUS team for their important contributions to the development of the experimental equipment, to J. Ledermann for his help in the mechanical design of the measurement station, and to C. Pralong for the valuable initial support.

References

1) *Guidebook on Non-Destructive Examination of Water Reactor Fuel*, IAEA-TECDOC-322 (1991).
2) H. Toubon *et al.*, *Burn-up Measurements Coupling Gamma Spectrometry and Neutron Measurement*, CANBERRA Tech. Doc. (2003).
3) J. R. Phillips, *Passive Nondestructive Assay of Nuclear Materials*, LA-UR-90-732, 529–562 (1991).
4) R. H. Tanke, J. E. Jasper, P. A. M. Gaalman, D. Killian, "Applications of tomography in nuclear research," *Kerntechnik*, **56**[5], 283–289 (1991).
5) T. Craciunescu, C. Niculae, G. Mateescu, C. Turcanu, "A comparison of four tomographic methods for nuclear fuel pin analysis," *J. Nucl. Mater.*, **224**[3], 199–206 (1995).
6) R. Dobrin, T. Craciunescu, I. L. Tuturici, "The analysis of failed nuclear fuel rods by gamma computed tomography," *J. Nucl. Mater.*, **246**[1], 37–42 (1997).
7) D. C. Camp, H. E. Martz, G. P. Roberson, D. J. Decman, R. T. Bernardi, "Nondestructive waste-drum assay for transuranic content by gamma-ray active and passive computed tomography," *Nuc. Instrum. Methods A*, **495**[1], 69–83 (2002).
8) C. Pralong Fauchere, F. Jatuff, M. Murphy, R. Chawla, "Adapting and applying SPECT to the investigation of reaction rate distribution within lightly activated nuclear fuel pins," *Nucl. Instrum. Methods A*, **522**[3], 579–590 (2004).
9) S. Jacobsson, A. Håkansson, A. Bäcklin, O. Osifo, C. Willman, P. Jansson, "Nondestructive experimental determination of the pin-power distribution in nuclear fuel assemblies," *Nucl. Sci. & Eng.*, **151**[1], 70–76 (2005).
10) M. Murphy, F. Jatuff, P. Grimm, R. Seiler, R. Brogli, G. Meier, H. Berger, R. Chawla, "Reactivity and neutron emission measurements of burnt PWR fuel rod samples in LWR-PROTEUS Phase II," *Ann. Nuc. En.*, **33**, 760–765 (2006).
11) *DSPEC™. Digital Gamma-Ray Spectrometer*, EG&G ORTEC Catalog, Oak Ridge.
12) *Gamma-VisionTM-32. Gamma-Ray Spectrum Analysis and MCA Emulation for Microsoft® Windows® 95 and Microsoft Windows NT. A66-B32 Software User's Manual*, EG&G ORTEC Part No. 774780 Manual Revision A, Oak Ridge (1998).
13) *Sentinel Gamma Ray Projector Model DELTA 880 Technical Manual*, AEA TECHNOLOGY, http://www.qsa-global.com/assets/Documents/MAN-027-880ManualMarch2004.pdf.
14) S. Caruso, *Characterisation of High-Burnup LWR Fuel Rods through Gamma Tomography*, Thèse EPFL No. 3762, 2007, http://library.epfl.ch/theses/?nr=3762.
15) S. Caruso, I. Günter-Leopold, M. Murphy, F. Jatuff, R. Chawla, "Validation of optimised germanium gamma spectrometry vs. multicollector inductively coupled plasma mass spectrometry for the determination of ^{134}Cs,^{137}Cs and ^{154}Eu single ratios in highly burnt UO_2," *Nucl. Instrum. Methods A* (2007) (accepted), [doi:10.1016/j.nima.2008.03.005].

16) G. T. Herman, *Image Reconstruction from Projections: The Fundamentals of Computerized Tomography*, Academic Press, New York (1980).
17) J. A. Fessler, A. O. Hero, "Space-alternating generalized expectation-maximization algorithm," *IEEE Sig. Proc.*, **42**[10], 2664–2677 (1994).
18) H. Erdogan, J. A. Fessler, "Monotonic algorithms for transmission tomography," *IEEE Tr. Med. Im.*, **18**[9], 801–814 (1999).
19) J. Radon, "Über die Bestimmung von Funktionen durch ihre Intergralwerte langs gewisser Mannigfaltigkeiten (On the determination of functions from their integrals along certain manifolds)," *Berichte Sächsische Akademie der Wissenschaften*, **29**, 262–277 (1917).
20) L. A. Shepp, Y. Vardi, "Maximum likelihood reconstruction for emission tomography," *IEEE Trans. Med. Imaging*, **1**[2], 113–122 (1982).
21) K. Lange, R. Carson, "EM reconstruction algorithms for emission and transmission tomography," *Jour. Comp Assisted Tomogr.*, **8**[2], 306–316 (1984).
22) J. A. Fessler, *Aspire 3.0 User's Guide: A Sparse Iterative Reconstruction Library*, Technical Report No. 293 Communications & Signal Processing Laboratory, University of Michigan (2001).
23) A. Romano, M. I. Horvath, R. Restani, "Evolution of porosity in high-burnup fuel structure," *J. Nucl. Mater.*, **361**, 62–68 (2007).
24) W. Goll, C. Hellwig, P. B. Hoffmann, W. Sauser, J. Spino, C. T. Walker, "UO_2 fuel behaviour at rod burn-ups up to 105 MWd/kgHM," *Int. J. Nucl. Power*, **52**[2], 95–102 (2007).